



Cite this: *Catal. Sci. Technol.*, 2016, 6, 2150

# MeO<sub>x</sub>/Al<sub>2</sub>O<sub>3</sub> and MeO<sub>x</sub>/CeO<sub>2</sub> (Me = Fe, Co, Ni) catalysts for high temperature N<sub>2</sub>O decomposition and NH<sub>3</sub> oxidation†

L. G. Pinaeva,<sup>\*a</sup> I. P. Prosvirin,<sup>ab</sup> L. S. Dovlitova,<sup>a</sup> I. G. Danilova,<sup>a</sup> E. M. Sadovskaya<sup>ab</sup> and L. A. Isupova<sup>a</sup>

A series of MeO<sub>x</sub>/Al<sub>2</sub>O<sub>3</sub> and MeO<sub>x</sub>/CeO<sub>2</sub> (Me = Fe, Co, Ni) compounds was prepared by incipient wetness impregnation and characterized by XRD, XPS, UV-vis DRS, differential dissolution phase analysis (DDPA). Their activity towards N<sub>2</sub>O decomposition and ammonia oxidation at 750–900 °C was shown to depend on oxygen mobility in the sample as characterized by steady state isotopic transient kinetic analysis (<sup>18</sup>O SSITKA) and dispersion of MeO<sub>x</sub> (Me = Fe) species. Obvious reverse “activity-FeO<sub>x</sub> dispersion” dependence was related to the change of contribution from oxygen transfer from the support to active sites through the Me–ceria or not improbably, the Me–alumina interface. It was shown that the high efficiency of CeO<sub>2</sub> based samples in deN<sub>2</sub>O can be additionally increased by CeO<sub>2</sub> supporting onto high surface area alumina.

Received 21st August 2015,  
Accepted 24th October 2015

DOI: 10.1039/c5cy01381j

www.rsc.org/catalysis

## 1. Introduction

Secondary abatement processes of N<sub>2</sub>O formed as an undesirable by-product during the catalytic oxidation of ammonia into nitric oxide implicates a catalyst set up in the ammonia burner operating at 800–900 °C directly after the Pt–Rh gauzes.<sup>1</sup> Bulk or supported mixed metal oxides were developed for catalytic N<sub>2</sub>O decomposition and put into practice in nitric acid plants before 2000 (Co<sub>2</sub>AlO<sub>4</sub>/CeO<sub>2</sub>, CuO/Al<sub>2</sub>O<sub>3</sub>, La<sub>0.8</sub>Ce<sub>0.2</sub>CoO<sub>3</sub> and Fe/ZrO<sub>2</sub>).<sup>1</sup> Moreover, alternative catalytic formulations were evaluated such as yttrium-doped zirconia,<sup>2</sup> ceria–zirconia,<sup>3</sup> A<sub>1–x</sub>A'<sub>x</sub>B<sub>1–y</sub>B'<sub>y</sub>O<sub>3</sub> perovskites with A = La or Ca, B = Mn, Co or Fe, A' = Sr, B' = Cu or Ni,<sup>4–6</sup> metal-substituted hexa-aluminates,<sup>7</sup> Fe<sub>2</sub>O<sub>3</sub>–MeO<sub>x</sub> (Me = Al, Zr, Ce, La, Cu, Cr) obtained by co-precipitation,<sup>8,9</sup> Co<sub>3</sub>O<sub>4</sub> (ref. 10) and CoO<sub>x</sub>–CeO<sub>2</sub> (ref. 11) obtained by calcinations of mixtures of individual oxides. The pilot plant reactor and real plant studies<sup>8</sup> confirmed high activity and very good mechanical stability of the Fe<sub>2</sub>O<sub>3</sub>/Al<sub>2</sub>O<sub>3</sub> catalysts prepared by co-precipitation as well as no decomposition of nitric oxide. Several aspects with respect to the reaction mechanisms, the structure–activity correlations, the role of various gas inhibitors as well as the strategies followed to adjust the local surface structure of the abovementioned noble metal-free metal oxides were analyzed in the review of Konsolakis.<sup>12</sup>

Ageing of Pt–Rh gauzes is accompanied by decrease of activity and yield of NO + NO<sub>2</sub> (NO<sub>x</sub>), whereas N<sub>2</sub>O production increases. Taking account of the tendency in the last decade to reduce platinum metal loading in the reactor (including the number of gauzes and wire thicknesses), at gauzes deactivation noticeable slip of ammonia becomes possible followed by its reaction with NO<sub>x</sub>. Therefore, development of a bi-functional catalyst that is capable of efficient N<sub>2</sub>O abatement and NH<sub>3</sub> oxidation to NO<sub>x</sub> becomes urgent for further optimization and the reduction of harmful emissions from the process of HNO<sub>3</sub> production.

An idea for development of an oxide-based catalyst that is capable of converting slipping ammonia with high selectivity to NO<sub>x</sub> was successfully realized using a dual bed system, in which a Fe<sub>2</sub>O<sub>3</sub>–Al<sub>2</sub>O<sub>3</sub>-based extruded monolith followed fewer numbers of platinum gauzes.<sup>13</sup> Later studies showed the efficiency of these compositions in both slipping NH<sub>3</sub> oxidation to NO<sub>x</sub> and N<sub>2</sub>O abatement.<sup>14</sup> At the same time, Al<sub>2</sub>O<sub>3</sub>-based honeycomb catalysts with the same geometry and FeO<sub>x</sub>-based active components supported by impregnation were substantially more active in both reactions and retained high activity after the run in a dual-bed system for 3 months.<sup>14</sup>

Earlier, we have shown that catalytic activity of Sr substituted La manganites in high-temperature N<sub>2</sub>O decomposition correlated with the coefficient of lattice oxygen self-diffusion.<sup>5</sup> In the materials with high bulk oxygen mobility, the rates of oxygen transfer in the two-phase system “O<sub>2(gas)</sub>–surface–catalyst bulk” characterized by <sup>16</sup>O/<sup>18</sup>O exchange and N<sub>2</sub>O decomposition additionally increased either by their decoration by structures characterized by a

<sup>a</sup> Borekov Institute of Catalysis, Novosibirsk, Russia. E-mail: pinaeva@catalysis.ru

<sup>b</sup> Novosibirsk State University, Novosibirsk, Russia

† Electronic supplementary information (ESI) available. See DOI: 10.1039/c5cy01381j

higher rate of heteroexchange (composites LaSrFeO<sub>4</sub> (surface)–La<sub>0.4</sub>Sr<sub>0.6</sub>FeO<sub>3</sub> (bulk)<sup>6</sup>) or by modification of near surface layers by hetero-cations (LaFeO<sub>3</sub>–CeO<sub>2</sub> composites with Fe<sup>3+</sup> ions inserted into a fluorite lattice<sup>15</sup>). In the former case,<sup>6</sup> “activity – oxygen mobility” correlation was observed for reaction of NH<sub>3</sub> oxidation as well. Pérez-Ramírez *et al.*<sup>16</sup> showed that the reaction of NH<sub>3</sub> oxidation to NO<sub>x</sub> over oxide catalysts (Fe<sub>2</sub>O<sub>3</sub>, CeO<sub>2</sub>, Cr<sub>2</sub>O<sub>3</sub>) follows a Mars–van Krevelen-type scheme with participation of lattice oxygen and reoxidation of the so-formed vacancies by both gas-phase O<sub>2</sub> and bulk lattice oxygen. Due to this, the efficiency of NH<sub>3</sub> oxidation to NO<sub>x</sub>, especially in oxygen deficient conditions, depended on the rate of bulk oxygen diffusion to surface vacancies.

In accordance with these findings, the idea to combine high activity towards N<sub>2</sub>O decomposition and NH<sub>3</sub> oxidation (at high selectivity to NO<sub>x</sub>) in the same sample was checked. In addition to Fe/Al<sub>2</sub>O<sub>3</sub>(CeO<sub>2</sub>) samples, Co- and Ni- supported on Al<sub>2</sub>O<sub>3</sub> and CeO<sub>2</sub> were tried as well since a vast number of patent applications have claimed a relatively high NO selectivity (90–95%) using Co and Ni single metal oxides. Numerous attempts were made to commercialize Co<sub>3</sub>O<sub>4</sub>-based catalysts but substantially lower activity and reversible deactivation of Co-systems, due to reduction of Co<sub>3</sub>O<sub>4</sub> by NH<sub>3</sub> to the inactive CoO under reaction conditions in the upper parts of the bed, excluded the replacement of Pt gauzes by oxide catalysts. Nevertheless, these systems could be tried as the second catalyst in the dual bed system, especially since the stabilizing effect of CeO<sub>2</sub> in Co<sub>3</sub>O<sub>4</sub>–CeO<sub>2</sub> mixed oxides with low Co content is well-known.<sup>11</sup> Since copper catalyzes ammonium nitrate decomposition, an extremely important safety problem may arise if copper leaches from the catalyst and accumulates in the fertilizer product.<sup>1</sup> This completely excludes any Cu-based system for use in the conditions of the ammonia burner, although Cu/CeO<sub>2</sub> revealed high efficiency in deN<sub>2</sub>O at lower temperatures<sup>17,18</sup> and more probably can be located after the absorption column. In addition, it is well known that under these conditions, Cu-containing systems oxidize NH<sub>3</sub> to N<sub>2</sub> with high selectivity.

In the first stage, we showed that intrinsic catalytic activity of different Me/Al<sub>2</sub>O<sub>3</sub> (Me = Fe, Co, Ni) samples obtained by impregnation towards N<sub>2</sub>O decomposition and NH<sub>3</sub> oxidation was substantially lower compared to corresponding Me/CeO<sub>2</sub> samples with similar surface Me concentration and correlated with the rate of oxygen exchange in the samples. Variation of Fe content in the Fe/Al<sub>2</sub>O<sub>3</sub>(CeO<sub>2</sub>) samples revealed noticeable reverse dependence of deN<sub>2</sub>O and NH<sub>3</sub> oxidation activity due to the size effect. In accordance with this, we supported FeO<sub>x</sub> onto specially developed Al<sub>2</sub>O<sub>3</sub><sup>19</sup> characterized by high specific surface area, and formation of highly dispersed FeO<sub>x</sub> at increased Fe content in the sample finally resulted in N<sub>2</sub>O and NH<sub>3</sub> conversion increase. For such samples, we focused on Fe oxide as the active component because in the case of Me = Co, Ni low active MeAl<sub>2</sub>O<sub>4</sub> or NiO<sub>x</sub> phases were formed on the alumina surface. Using of the effect of high oxygen mobility in CeO<sub>2</sub> was restricted by

its low surface area at the temperature of reaction, independently on preparation method.<sup>3,11,20</sup> Therefore, an attempt was made to disperse CeO<sub>2</sub> using precipitation onto high surface area Al<sub>2</sub>O<sub>3</sub>.

## 2. Experimental

### 2.1. Sample preparation

CeO<sub>2</sub> and Al<sub>2</sub>O<sub>3</sub> samples used as the support were obtained by calcination of the corresponding nitrates of chemical purity (99.5%) at 900 °C for 36 h. Al<sub>2</sub>O<sub>3</sub>-based supports were prepared by calcination of: 1) Al(NO<sub>3</sub>)<sub>3</sub>·9H<sub>2</sub>O of chemical purity (99.5%) at 1000 °C or 1200 °C for 6 h (denoted below as Al<sub>2</sub>O<sub>3</sub>-1000 and Al<sub>2</sub>O<sub>3</sub>-1200, respectively), or 2) the product of centrifugal thermal activation of commercial-grade alumina hydrate (hydrargillite)<sup>19</sup> at 1000 °C for 19 h (Al<sub>2</sub>O<sub>3</sub>-C). To obtain the Ce/Al<sub>2</sub>O<sub>3</sub> support, the product of thermochemical activation of hydrargillite was first calcined at 500 °C (*S*<sub>BET</sub> = 210 m<sup>2</sup> g<sup>−1</sup>); then, CeO<sub>2</sub> was precipitated onto this product from 0.75 M Ce(NO<sub>3</sub>)<sub>3</sub>·6H<sub>2</sub>O water solution using 1 M (NH<sub>4</sub>)<sub>2</sub>CO<sub>3</sub> as a precipitation agent, so that the Ce:Al ratio in the final product was 1:1 (mole). The resultant precipitate was washed until the pH of the filtrate was 7, dried at 60 °C overnight, followed by calcination at 900 °C for 5 h.

All Me/support samples (Me = Fe, Co, Ni) were prepared by incipient wetness impregnation of the corresponding support by water solution of Me nitrate with added citric acid in 10 wt% excess to the stoichiometric amount to form the corresponding citrates and ethyleneglycol, dried in air at 150 °C for 3 h and then calcined at 900 °C for 4 h. In the commonly-used abbreviation *n*Me/support, “*n*” corresponded to Me weight content in the sample in terms of the corresponding metal, although oxide compounds obviously formed. For CeO<sub>2</sub> and Al<sub>2</sub>O<sub>3</sub>-1200, the samples with Me concentration 6.7 × 10<sup>19</sup> at m<sup>−2</sup> have been prepared, which corresponded to Me content of around 2.5–2.7 wt% (Al<sub>2</sub>O<sub>3</sub>-1200) and 0.86–0.91 wt% (CeO<sub>2</sub>). For all supports, we also varied Fe content in the samples from 0.86 to 19.8 wt%. Bulk MeO<sub>x</sub> were obtained by calcination of the corresponding chemical purity nitrates at 900 °C for 6 h.

### 2.2. Sample characterization

X-ray powder diffraction (XRD) patterns were recorded using a Bruker D8 diffractometer with Cu K<sub>α</sub> monochromatic radiation. Each sample was scanned in the range of 2θ from 10° to 70° with a step size of 0.05° in 2θ. Surface composition of the samples was investigated by X-ray photoelectron spectroscopy (XPS) using a SPECS spectrometer with Al-K<sub>α</sub> irradiation (*hν* = 1486.6 eV). The binding energy (BE) scale was preliminarily calibrated by the position of the peaks of Au 4f<sub>7/2</sub> (84.0 eV) and Cu 2p<sub>3/2</sub> (932.67 eV) core levels. UV-vis diffuse reflectance spectra (UV-vis DRS) were obtained using a UV-2501 PC Shimadzu spectrometer with an IRS-250A diffusion reflection attachment in the 11 000–54 000 cm<sup>−1</sup> range using BaSO<sub>4</sub> as a reference. The edge energy (or band gap, *E<sub>g</sub>*) for allowed transitions was determined by finding the intercept of the



straight line for the low-energy rise of a plot of  $[F(R_{\infty})/hv]^2$  versus  $hv$ ,<sup>21</sup> where  $hv$  is the incident photon energy and  $F(R_{\infty})$  is the Kubelka–Munk function.

The method of differential dissolution phase analysis (DDPA) was used to reveal the composition of the phases (including poorly crystallized, but without information about the oxygen content therein) formed in the supported samples, including possible decoration of one phase by another.<sup>22</sup> For this, about 10 mg of the sample was loaded in a microreactor and dissolved in the water based solvent with the composition changing from the lower towards higher acidity in the following order: 1) HCl (pH = 2), 2) (1 ÷ 3) M HCl, while the temperature increased continuously from 20 °C to 90 °C, 3) (3.6 M) HF and running the reactor with a flow rate of 3.6 ml min<sup>-1</sup>. Change of the outlet mixture composition with time was analyzed by atomic emission spectroscopy (BAIRD spectrometer) using the following spectral lines (nm) of the elements: Fe–238.2, Al–308.2, Ce–413.8, Co–238.8 with 5% accuracy of measurements at sensitivity level 10<sup>-3</sup> µg ml<sup>-1</sup>.

Kinetics of oxygen exchange was characterized by steady state isotopic transient kinetic analysis (SSITKA). For SSITKA experiments, the sample ( $g = 0.025$  g) was loaded into a reactor (quartz tube, i.d. = 3 mm) and heated to 800 °C in an 0.5% vol. <sup>16</sup>O<sub>2</sub> + He flow and kept at this temperature for 30 minutes, whereupon the gas mixture was replaced stepwise by the same one containing <sup>18</sup>O<sub>2</sub> and Ar (1 vol%) as an inert tracer. The gas flow rate for all mixtures amounted to 16.7 cm<sup>3</sup> s<sup>-1</sup>. All responses were analyzed as time variation of the <sup>18</sup>O atomic fraction in the gas phase  $\alpha_g(t) = (^{16}\text{O}^{18}\text{O} + 2^{18}\text{O}_2)/(2\Sigma\text{O}^i\text{O}^j)$ , where  $\Sigma\text{O}^i\text{O}^j = ^{16}\text{O}_2 + ^{16}\text{O}^{18}\text{O} + ^{18}\text{O}_2$ .<sup>23</sup>

The catalytic activity for samples with particles of 250–500 µm in size was measured in a fixed-bed U-shaped reactor (3 mm i.d. quartz tube) at ambient pressure in the temperature range 750–900 °C and contact time  $\sim 10^{-3}$  s. For NH<sub>3</sub> oxidation, a mixture of 1% NH<sub>3</sub> in air or 1% NH<sub>3</sub> + 2% O<sub>2</sub> in N<sub>2</sub> was fed to the reactor charged by 0.015 or 0.043 g of the sample (see details in the text) with a flow rate 25 l h<sup>-1</sup>. Outlet mixture composition was measured by IR spectroscopy. For N<sub>2</sub>O decomposition, a gas mixture consisting of 0.15 vol% N<sub>2</sub>O (+3% O<sub>2</sub> + 3% H<sub>2</sub>O) in He flowed through the reactor with a flow rate of 60 l h<sup>-1</sup>. For samples characterized by high specific surface area (Al<sub>2</sub>O<sub>3</sub>-C, Ce/Al<sub>2</sub>O<sub>3</sub> based), we failed to reach reasonably low values of N<sub>2</sub>O conversion at 800 °C. Therefore, the data obtained at the same sample loading (0.038 g) and flow rate (60 l h<sup>-1</sup>) were considered to analyze the effect of Fe concentration. Outlet mixture composition was analyzed by an on-line gas chromatograph with Porapack T (i.d. = 3 mm, l = 3 m) and NaX (i.d. = 3 mm, l = 2 m) columns.

## 3. Results and discussion

### 3.1. Phase composition

**3.1.1. XRD analysis.** Al<sub>2</sub>O<sub>3</sub>-1200 (Fig. 1a), Al<sub>2</sub>O<sub>3</sub>-1000 and CeO<sub>2</sub> used as the supports were single phase samples

(Table 1), with values of coherent scattering area  $d_{\text{XRD}}$  calculated by the Scherrer equation much less than the particle size estimated from the BET surface area ( $d_{\text{BET}}$ ). For example, for Al<sub>2</sub>O<sub>3</sub>-1200  $d_{\text{XRD}} = 360$  Å,  $d_{\text{BET}} = 3800$  Å, while for CeO<sub>2</sub>-680 Å and 6400 Å. TEM images of the CeO<sub>2</sub> sample revealed a mixture of agglomerates composed of concreted crystallites of either 100 nm or 10 nm in size.<sup>15</sup> The same can be reasonably supposed for Al<sub>2</sub>O<sub>3</sub>-1200 and Al<sub>2</sub>O<sub>3</sub>-1000 samples as well to explain the difference between  $d_{\text{BET}}$  and  $d_{\text{XRD}}$  values. Al<sub>2</sub>O<sub>3</sub>-C represented a mixture of  $\alpha$ -Al<sub>2</sub>O<sub>3</sub> (Fig. 1B, Table 1) with more dispersed  $\theta$ -Al<sub>2</sub>O<sub>3</sub>,  $\gamma$ -Al<sub>2</sub>O<sub>3</sub> and traces of  $\kappa$ -Al<sub>2</sub>O<sub>3</sub>. In the Ce/Al<sub>2</sub>O<sub>3</sub> sample, CeO<sub>2</sub> phase with the same lattice parameters but expected more dispersed, than in CeO<sub>2</sub> sample, species,  $\theta$ -Al<sub>2</sub>O<sub>3</sub> and traces of  $\gamma$ -Al<sub>2</sub>O<sub>3</sub> were detected (Fig. 1C, Table 1). Dispersion of the  $\theta$ -Al<sub>2</sub>O<sub>3</sub> species was about the same as in Al<sub>2</sub>O<sub>3</sub>-C, as follows from similar widening of peaks at  $2\theta$  of  $\sim 67^\circ$  ( $\gamma$ -Al<sub>2</sub>O<sub>3</sub> +  $\theta$ -Al<sub>2</sub>O<sub>3</sub>), but cannot be calculated more precisely because of overlapping of its more intense peak at  $2\theta \sim 32.9^\circ$  with that of CeO<sub>2</sub>.

Although Co<sub>3</sub>O<sub>4</sub> and Co–Al–O spinels are characterized by the same symmetry group, increased lattice parameters of Co compounds in 2.7Co/Al<sub>2</sub>O<sub>3</sub>-1200 sample (Fig. 1A) ( $a = b = c = 8.104$  (1) Å) compared with those in the 0.91Co/CeO<sub>2</sub> one or in bulk Co<sub>3</sub>O<sub>4</sub> ( $a = b = c = 8.084$  (0) Å) favor formation of CoAl<sub>2</sub>O<sub>4</sub> in the former,<sup>24</sup> probably in the mixture with Co<sub>3</sub>O<sub>4</sub>. In the 2.7Ni/Al<sub>2</sub>O<sub>3</sub>-1200 and 2.5Fe/Al<sub>2</sub>O<sub>3</sub>-1200 samples, additional NiO with admixture of highly dispersed Ni–Al–O compounds of spinel structure and  $\alpha$ -Fe<sub>2</sub>O<sub>3</sub>, respectively, were detected. The lattice parameters of NiO and Fe<sub>2</sub>O<sub>3</sub> in the supported samples were exactly the same as for bulk MeO<sub>x</sub> (not presented in Table 1 for clarity). However, slight increase of  $\alpha$ -Al<sub>2</sub>O<sub>3</sub> lattice parameters in all Me/Al<sub>2</sub>O<sub>3</sub> samples points to the probability of non-substantial Me<sup>n+</sup> penetration into the alumina lattice. Taking account of the slightly larger radii of Me<sup>3+</sup> ions compared with that of Al<sup>3+</sup> (69–74 pm and 67.5 pm, respectively), such an assumption looks quite reasonable.

FeO<sub>x</sub> supported on Al<sub>2</sub>O<sub>3</sub>-C resulted in continuous decrease of the peaks corresponding to  $\theta$ -,  $\kappa$ -,  $\gamma$ -Al<sub>2</sub>O<sub>3</sub> with an increase of Fe content from 2.5 to 13.2 wt% (Fig. 1b). Instead of these, a second  $\alpha$ -Al<sub>2</sub>O<sub>3</sub> phase with an increased lattice parameter ( $a = b = 4.795$  Å,  $c = 13.057$  Å) becomes evident and increases in intensity (Table 1), which more obviously points to efficient incorporation of Fe<sup>3+</sup> ions into the lattices of low temperature aluminas thus promoting their transition to  $\alpha$ -Al<sub>2</sub>O<sub>3</sub> at a lower temperature.<sup>25</sup> This fact agrees well with decrease of  $S_{\text{BET}}$  value from 70 m<sup>2</sup> g<sup>-1</sup> for Al<sub>2</sub>O<sub>3</sub>-C to 22 m<sup>2</sup> g<sup>-1</sup> after supporting 19.8% of Fe (pattern of the last sample not presented for brevity).

In the patterns of (0.86–0.91)Me/CeO<sub>2</sub> samples, traces of crystalline MeO<sub>x</sub> were observed only for the case of Me = Co, and some  $\alpha$ -Fe<sub>2</sub>O<sub>3</sub> was detected for substantially higher Fe content (sample 2.5Fe/CeO<sub>2</sub>). Nevertheless, unlike alumina-based samples, neither sintering of CeO<sub>2</sub> nor change of CeO<sub>2</sub> lattice parameters were noted after Me supporting (Table 1). Considering that the radius of Fe<sup>3+</sup> ions (0.049–0.078 pm,



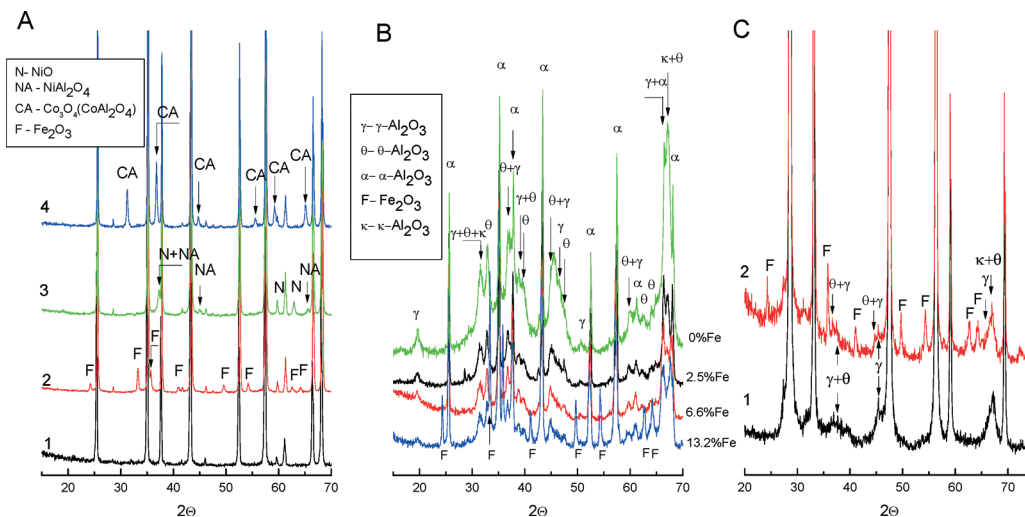


**Fig. 1** XRD patterns of: (A)  $\text{Al}_2\text{O}_3$ -1200 (1) and (2.5–2.7) Me/ $\text{Al}_2\text{O}_3$ -1200 (Me = Co(4), Fe (2), Ni(3)) samples, (B) Fe/ $\text{Al}_2\text{O}_3$ -C samples with different Fe content, and (C) Ce/ $\text{Al}_2\text{O}_3$  (1) and 9.9Fe/Ce/ $\text{Al}_2\text{O}_3$  (2) samples.

depending on coordination and spin state) is smaller than that of  $\text{Ce}^{4+}$  ions in the typical cubic fluorite lattice (0.097–0.101 nm), the expected lattice shrinkage took place at substantial Fe content in the mixed  $\text{Fe}_x\text{-Ce}_{1-x}$  oxides.<sup>26</sup> However, at  $x < 0.05$ , even slight unit cell expansion was observed and related by authors to partial  $\text{Ce}^{4+}$  reduction to the larger (1.23 Å)  $\text{Ce}^{3+}$  ion<sup>27</sup> during calcination in the presence of  $\text{Fe}^{3+}$ . Therefore, penetration of supporting Me into the  $\text{CeO}_2$  lattice cannot be excluded, especially taking account of concreted nanocrystallites present in the initial support.

In the 9.9Fe/Ce/ $\text{Al}_2\text{O}_3$  sample,  $\alpha\text{-Fe}_2\text{O}_3$  was detected with lattice parameters and  $d_{\text{XRD}}$  value similar to that in 13.2Fe/ $\text{Al}_2\text{O}_3$ -C and 2.5Fe/ $\text{Al}_2\text{O}_3$ -1200 samples. Although Fe supporting onto Ce/ $\text{Al}_2\text{O}_3$  resulted in noticeable drop of the surface area, like in  $\text{Al}_2\text{O}_3$ -C based samples, it did not facilitate formation of  $\alpha\text{-Al}_2\text{O}_3$  (Tables 1 and 2, Fig. 1C). For similar  $\text{CeO}_2$ / $\text{Al}_2\text{O}_3$  samples, it was shown that it is Ce in the lower oxidation state that stabilizes alumina toward the formation of low surface area phases up to 1100 °C or 1200 °C under oxidizing and reducing conditions, respectively.<sup>28</sup> Since CeAlO<sub>3</sub> crystallites at high temperature and under reducing conditions were observed by XRD, stabilization of  $\text{Ce}^{3+}$  is more probably due to interaction with the OH groups of alumina. Absence of such alumina-bonded hydroxyl groups can prevent penetration of  $\text{Fe}^{3+}$  into the bulk alumina and the phase transition observed in the case of the  $\text{Al}_2\text{O}_3$ -C sample.

**3.1.2. DDPA.** DDPA of (2.5–2.7)Me/ $\text{Al}_2\text{O}_3$ -1200 and (0.86–0.91) Me/ $\text{CeO}_2$  samples has been performed to reveal 1) possible modification of support lattice due to Me insertion, and 2) formation of Co–Al spinels.  $\text{Al}_2\text{O}_3$ -1200 supported samples were quite stable towards dissolution. Therefore, about 5 wt% and 2 wt% of the 2.5Fe/ $\text{Al}_2\text{O}_3$ -1200 and 2.7Co/ $\text{Al}_2\text{O}_3$ -1200 samples, respectively, dissolved during all steps (Table 2). Nevertheless, all Fe supported onto  $\text{Al}_2\text{O}_3$ -1200 passed into solution (Fig. 2A) as individual oxide/hydroxide (about 18.4

mole% of the probe dissolved in HCl), or together with some Al (~43.5 mole% of the probe dissolved in HF). Since some dissolution proceeded even after all Fe was removed from the sample, formation of Fe–Al solid solution is excluded, and the structure with  $\text{FeO}_x$  species located on the surface or on the intergrain boundaries of concreted alumina microcrystallites and linked to the last, more probably, due to penetration of some  $\text{Fe}^{3+}$  ions to the disordered near subsurface layers can be considered. In the case of 2.7Co/ $\text{Al}_2\text{O}_3$ -1200, only 0.43 wt% of Co dissolved in all steps, an overwhelming majority, as the solid solution with  $\text{Co}_{0.3}\text{Al}_1$  stoichiometry reasonably relates to the mixed Co–Al–O spinel like compounds located in the near surface layer of the sample. The nature of insoluble Co compounds still remains unclear.

$\text{CeO}_2$  did not dissolve in HCl, and very slow dissolution (about 4% of the total sample weight in 7 minutes) took place after HF feeding (Fig. 2B, Table 2). Me/ $\text{CeO}_2$  samples dissolved in substantially milder conditions, but the character and the rate of their dissolution depended on the nature of Me. Therefore, already 95 weight% of the 0.91Co/ $\text{CeO}_2$  sample dissolved in these conditions. Increase of solubility can be related first of all to formation of Co–Ce–O solid solution with Co/Ce = 0.004 and including all soluble Ce (dissolved in (1 ÷ 3) M HCl). This obviously means that  $\text{Co}^{3+}$  ions are able to insert into more dispersed (~10 nm) concreted microcrystallites and modify the lattice of larger (~100 nm) particles increasing their solubility. The rest of Co dissolved slowly as an oxide in the most harsh conditions (3.6 M HF) and more probably, can be related to the well-crystallized  $\text{Co}_3\text{O}_4$  detected by XRD (Table 1). Absence of any Co in the same flow during dissolution of the 2.7Co/ $\text{Al}_2\text{O}_3$ -1200 sample points to the formation of well-crystallized Co–Al spinel therein. The quantity of 0.86Fe/ $\text{CeO}_2$  sample dissolved was somewhat lower (54 wt% of the total) and all Fe passed into solution as it was found for 2.5Fe/ $\text{Al}_2\text{O}_3$ -1200 sample (Fig. S1†). It was included into Fe oxide/





**Table 1** BET surface area, phase composition, structural parameters, and crystallite size estimated from XRD ( $d_{\text{XRD}}$ ) of  $\text{Al}_2\text{O}_3$ ,  $\text{CeO}_2$  and  $\text{MeO}_x/\text{CeO}_2(\text{Al}_2\text{O}_3)$  samples

Sample	$S_{\text{BET}}$ , $\text{m}^2 \text{g}^{-1}$	Phase composition	$d_{\text{XRD}}$ , Å
$\text{Al}_2\text{O}_3$ -1200	4	$\alpha\text{-Al}_2\text{O}_3$ ( $a = b = 4.756$ Å, $c = 12.986$ Å)	370
$\text{Al}_2\text{O}_3$ -1000	7	$\alpha\text{-Al}_2\text{O}_3$ ( $a = b = 4.760$ Å, $c = 12.997$ Å)	300
$\text{Al}_2\text{O}_3$ -C	71	$\alpha\text{-Al}_2\text{O}_3$ ( $a = b = 4.771$ Å, $c = 13.020$ Å)	480
		$\theta\text{-Al}_2\text{O}_3$ , $\kappa\text{-Al}_2\text{O}_3$ , $\gamma\text{-Al}_2\text{O}_3$	100 ( $\gamma\text{-Al}_2\text{O}_3$ ), 140 ( $\theta\text{-Al}_2\text{O}_3$ )
2.5Fe/ $\text{Al}_2\text{O}_3$ -1200	4.0	$\alpha\text{-Fe}_2\text{O}_3$ ( $a = b = 5.035(0)$ Å, $c = 13.741$ Å)	260
		$\alpha\text{-Al}_2\text{O}_3$ ( $a = b = 4.761$ Å, $c = 12.997$ Å)	500
2.7Co/ $\text{Al}_2\text{O}_3$ -1200	4.0	$\text{CoAl}_2\text{O}_4$ or $\text{Co}_3\text{O}_4$ ( $a = b = c = 8.104$ Å)	260
		$\alpha\text{-Al}_2\text{O}_3$ ( $a = b = 4.761$ Å, $c = 12.997$ Å)	520
2.7Ni/ $\text{Al}_2\text{O}_3$ -1200	4.0	NiO ( $a = b = c = 4.178$ Å)	240
		$\text{NiAl}_2\text{O}_4$	$\leq 120$
		$\alpha\text{-Al}_2\text{O}_3$ ( $a = b = 4.760$ Å, $c = 12.996$ Å)	580
2.5Fe/ $\text{Al}_2\text{O}_3$ -C	60	$\alpha\text{-Al}_2\text{O}_3$ ( $a = b = 4.778$ Å, $c = 13.039$ Å)	510
		$\theta\text{-Al}_2\text{O}_3$ , $\kappa\text{-Al}_2\text{O}_3$ , $\gamma\text{-Al}_2\text{O}_3$	Highly dispersed
6.6Fe- $\text{Al}_2\text{O}_3$ -C	46	$\alpha\text{-Al}_2\text{O}_3$ : 31% - $a = b = 4.770$ Å, $c = 13.030$ Å	510
		69% - $a = b = 4.795$ Å, $c = 13.057$ Å	470
		$\theta\text{-Al}_2\text{O}_3$ , $\kappa\text{-Al}_2\text{O}_3$ , $\gamma\text{-Al}_2\text{O}_3$	Highly dispersed
13.2Fe- $\text{Al}_2\text{O}_3$ -C	33	$\alpha\text{-Al}_2\text{O}_3$ : 18% - $a = b = 4.760$ Å, $c = 13.000$ Å,	510
		82% - $a = b = 4.795$ Å, $c = 13.057$ Å,	520
		Traces of $\theta\text{-Al}_2\text{O}_3$ , $\kappa\text{-Al}_2\text{O}_3$ , $\gamma\text{-Al}_2\text{O}_3$	Highly dispersed
		$\text{Fe}_2\text{O}_3$ ( $a = b = 5.032$ Å, $c = 13.702$ Å)	250
$\text{CeO}_2$	1.4	$\text{CeO}_2$ ( $a = b = c = 5.412$ Å)	680
0.91Co/ $\text{CeO}_2$	1.4	$\text{CeO}_2$ ( $a = b = c = 5.412$ Å)	630
		$\text{Co}_3\text{O}_4$ ( $a = b = c = 8.084$ Å)	460
0.86Fe/ $\text{CeO}_2$	1.4	$\text{CeO}_2$ ( $a = b = c = 5.411$ Å)	550
0.91Ni/ $\text{CeO}_2$	1.4	$\text{CeO}_2$ ( $a = b = c = 5.411$ Å)	600
2.5Fe/ $\text{CeO}_2$	1.4	$\text{CeO}_2$ ( $a = b = c = 5.412$ Å)	650
		traces $\alpha\text{-Fe}_2\text{O}_3$	—
$\text{CeO}_2/\text{Al}_2\text{O}_3$	63	$\text{CeO}_2$ ( $a = b = c = 5.411$ Å)	400
		$\theta\text{-Al}_2\text{O}_3$ and traces of $\gamma\text{-Al}_2\text{O}_3$	Highly dispersed
9.9Fe/Ce/ $\text{Al}_2\text{O}_3$	35	$\text{CeO}_2$ ( $a = b = c = 5.411$ Å)	460
		$\theta\text{-Al}_2\text{O}_3$ and traces of $\gamma\text{-Al}_2\text{O}_3$	Highly dispersed
		$\alpha\text{-Fe}_2\text{O}_3$ ( $a = b = 5.035$ Å, $c = 13.741$ Å)	320

**Table 2** Chemical composition of dissolvable part of  $\text{Me}/\text{Al}_2\text{O}_3$ -1200( $\text{CeO}_2$ ) samples ( $\text{Me} = \text{Co}, \text{Fe}, \text{Ni}$ )

Sample	Sample dissolved, weight%	Me, weight% of the sample in dissolved portion	Element	Distribution of elements dissolved during different steps but O, mole%			
				Total	HCl (pH = 2)	0.33 M HCl	3.6 M HF
2.5Fe/ $\text{Al}_2\text{O}_3$ -1200	5	2.53	Al	38.1	—	—	38.1
			Fe	61.9	—	18.4	43.5
2.7Co/ $\text{Al}_2\text{O}_3$ -1200	2	0.43	Al	82.1	—	—	82.1
			Co	17.9	0.4	—	17.5
$\text{CeO}_2$	4	—	Ce	100	—	—	100
0.91Co/ $\text{CeO}_2$	95	0.93	Ce	98.2	—	98.2	—
			Co	1.8	Traces	0.39	1.41
0.86Fe/ $\text{CeO}_2$	54	1.0	Ce	96.8	—	96.8	—
			Fe	3.2	0.60	1.86	0.74
0.91Ni/ $\text{CeO}_2$	11	0.81	Ce	91.3	—	—	91.3
			Ni	8.7	Traces	7.8	0.9

hydroxide whose solubility in HCl (pH = 2) and at the substantially higher acidity (3.6 M HF) can be due to different degree of crystallinity or defect structures formed. The parallel dissolution of the remaining Fe and Ce in the flow of (1 ÷ 3) M HCl with the stoichiometry Fe/Ce = 0.02 points to formation of Fe–Ce–O solid solution, more probably, with participation of  $\text{CeO}_2$  composites characterized by smaller sizes of crystallites. Unmodified ceria is stable even in 3.6 M HF

and can be related to composites with largest crystallites. We cannot exclude that both unmodified  $\text{CeO}_2$  and Ce–Fe–O solid solution are decorated by highly defective Fe oxide/hydroxide species dissolved in weak HCl. In the case of the 0.91Ni/ $\text{CeO}_2$  sample (Fig. S1†), most of the supported Ni dissolved individually in (1 ÷ 3) M HCl, while the parallel Ni and Ce dissolution took place in the more rigid conditions (3 ÷ 6 M HF) and included only 10 weight% of the sample.



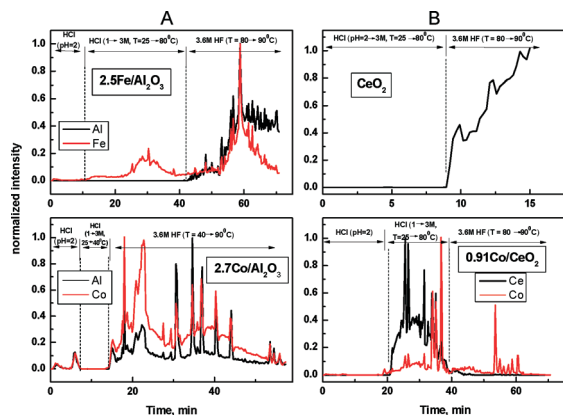


Fig. 2 DDPA spectra of: (A) 2.5Fe(2.7Co)/Al<sub>2</sub>O<sub>3</sub>-1200, (B) CeO<sub>2</sub> and 0.91Co/CeO<sub>2</sub> samples.

Therefore, in the 2.7Co/Al<sub>2</sub>O<sub>3</sub>-1200 sample, Al<sup>3+</sup> ions partially replace Co<sup>3+</sup> in the spinel structure, forming both highly disordered and well-crystallized Co–Al–O species, while incorporation of Fe<sup>3+</sup> ions into the boundaries of the micro-composites results in the anchoring of Fe<sub>2</sub>O<sub>3</sub> crystallites to the alumina surface. Me–ceria interaction results in formation of Me–Ce–O solid solutions in Me/CeO<sub>2</sub> samples; their content and degree of disorder in the sample change in the following order: 0.91Co/CeO<sub>2</sub> > 0.86Fe/CeO<sub>2</sub> > 0.91Ni/CeO<sub>2</sub> ≥ CeO<sub>2</sub>.

### 3.2. Microstructure

UV-vis DR spectra of different Co- and Fe-based catalysts have been presented in Fig. 3a and b, respectively. CeO<sub>2</sub> was characterized by strong absorbance bands at 36 500 and 29 000 cm<sup>−1</sup> attributed to Ce<sup>4+</sup> ← O<sup>2−</sup> charge transfer and the interband transitions, respectively,<sup>29</sup> and a band gap energy (*E<sub>g</sub>*) value of 3.35 eV, which is consistent with the reported value of 3.3 eV.<sup>29–31</sup> The spectra of 0.91Co/CeO<sub>2</sub> (Fig. 3a) and 0.86Fe/CeO<sub>2</sub> (Fig. 3b) samples are in fact a superposition of those for corresponding bulk oxides and CeO<sub>2</sub>, excluding the red shift of absorption edge of CeO<sub>2</sub> (*E<sub>g</sub>* values of 3.18 and 3.22 eV for 0.91Co/CeO<sub>2</sub> and 0.86Fe/CeO<sub>2</sub>, respectively) and additional absorption band at ~20 000 cm<sup>−1</sup> (Co case) and 23 500 cm<sup>−1</sup> (Fe case). A minimal red shift of the absorption edge compared to that in the support was found for the 0.91Ni/CeO<sub>2</sub> sample (*E<sub>g</sub>* value of 3.27 eV, spectrum not shown for brevity). We already observed these spectral characteristics for a Fe/CeO<sub>2</sub> sample prepared in the same way<sup>15</sup> and explained their appearance by O<sub>2</sub> adsorption on the structural defect, more obviously, clusters of oxygen vacancies arose after the entry of the dopant ions into the bulk of CeO<sub>2</sub>. As proposed in,<sup>30</sup> a change in the value of the absorption edge indicates that either (1) Me ions in Me/CeO<sub>2</sub> samples substitute into the CeO<sub>2</sub> lattice; or (2) the isolated Me ions form a mixed Me–Ce oxide and strongly interact with CeO<sub>2</sub> leading to the electronic structure changes. In our case, the value of the red shift correlated well with content

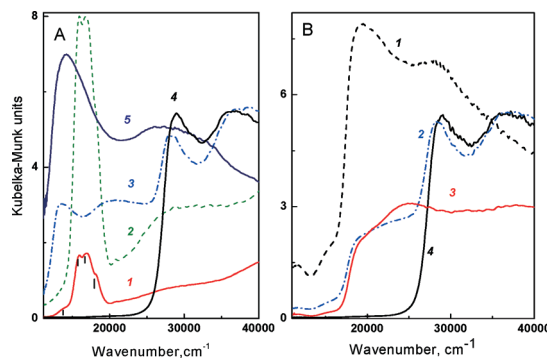


Fig. 3 UV-vis DR spectra of: A – (1) 2.9Co/Al<sub>2</sub>O<sub>3</sub>-1200, (2) CoAl<sub>2</sub>O<sub>4</sub> supplied by Aldrich, (3) 0.93Co/CeO<sub>2</sub>, (4) CeO<sub>2</sub>, (5) Co<sub>3</sub>O<sub>4</sub>; and B – (1) FeO<sub>x</sub>, (2) 0.86Fe/CeO<sub>2</sub>, (3) 2.7Fe/Al<sub>2</sub>O<sub>3</sub>-1200, (4) CeO<sub>2</sub>.

of Me–Ce mixed solution in the sample, as determined by DDPA.

In the spectrum of the 2.9Co/Al<sub>2</sub>O<sub>3</sub>-1200 sample, an intense triplet of bands at about 15 900, 17 000 and 18 200 cm<sup>−1</sup> with the shoulder at 13 800 cm<sup>−1</sup> was detected and related to the transitions of <sup>4</sup>A<sub>2</sub> → <sup>4</sup>T<sub>1</sub>(<sup>4</sup>P) of the tetrahedral Co<sup>2+</sup> ions in Co–Al–O spinel and cobalt oxide, respectively.<sup>32</sup> The presence of the same triplet in the reference CoAl<sub>2</sub>O<sub>4</sub> sample (Aldrich) supports formation of Co–Al–O spinel with admixture of Co<sub>3</sub>O<sub>4</sub>.

### 3.3. Surface composition

As follows from the X-ray photoelectron spectra of Ni 2p, Fe 2p, and Co 2p levels in Me/Al<sub>2</sub>O<sub>3</sub>-1200 and Me/CeO<sub>2</sub> samples presented in Fig. 4, the nature of Me surface compounds depends on the nature of the support. Usually, no difference between various Co compounds can be reliably drawn from binding energies of either Co 2p<sub>1/2</sub> or Co 2p<sub>3/2</sub> signals<sup>10</sup> without accounting for the position of their satellites arising due to the shake-up process of the Co<sup>2+</sup> compound in the high spin state. Indeed, BE values characterizing the Co 2p<sub>3/2</sub> peak position in CoO, CoOOH and Co<sub>3</sub>O<sub>4</sub> are indistinguishable (~780.0 eV). Higher, but also very close, BE values have been reported for CoAl<sub>2</sub>O<sub>4</sub> and Co(OH)<sub>2</sub> (781.9 and 781.2 eV, respectively).<sup>33–38</sup> However, for CoO, Co(OH)<sub>2</sub> or CoAl<sub>2</sub>O<sub>4</sub>, the satellite – main signal distances fall in the range 5–6.5 eV,<sup>34,35,39,40</sup> while the satellites in the spectrum of pure Co<sub>3</sub>O<sub>4</sub> and CoOOH should be located approximately 9–10 eV away from the main signals.<sup>34,36,39</sup> In this regard, the BE value of the Co 2p<sub>3/2</sub> signal at 781.6 eV with satellite at 786.6 eV in the 2.7Co/Al<sub>2</sub>O<sub>3</sub>-1200 sample (Fig. 4a) excluded CoO, Co<sub>3</sub>O<sub>4</sub> and CoOOH from our consideration, and either Co(OH)<sub>2</sub><sup>33</sup> or CoAl<sub>2</sub>O<sub>4</sub><sup>34,37,38</sup> could form on the surface. According to DDPA data, Co(OH)<sub>2</sub> could be responsible for about 0.4% of Co compounds (Table 2, corresponds to Co dissolved in HCl at pH = 2); therefore, most of the surface Co included in the Co–Al spinel structures. To ensure the correctness of such assignment, the spectrum of CoAl<sub>2</sub>O<sub>4</sub> supplied by Aldrich and additionally calcined at 900 °C for 5 h



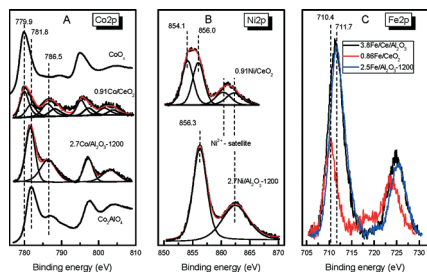


Fig. 4 (A) Co2p, (B) Ni2p, (C) Fe2p spectra of Me/Al<sub>2</sub>O<sub>3</sub>-1200(CeO<sub>2</sub>) samples (Me = Co, Ni, Fe) with similar ( $\sim 7 \times 10^{19}$  at/m<sup>2</sup>) concentration of Me, and Fe 2p spectrum of 3.8Fe/Ce/Al<sub>2</sub>O<sub>3</sub> sample (C).

has been presented as well. In the 0.91Co/CeO<sub>2</sub> sample, the position of the main Co 2p<sub>3/2</sub> peak shifted to lower BE values (779.9 eV), while the shoulder at 781.9 eV was still present resulting in the ratio of their intensities of  $\sim 3:2$ . Definite assignment of the peak at 779.9 eV to individual CoO, Co<sub>3</sub>O<sub>4</sub> or CoOOH was impossible since the presence of satellites at 786.7 and 790.8 eV agrees with formation of any of these compounds. In addition, in the XPS spectrum of the bulk Co<sub>3</sub>O<sub>4</sub> sample characterized by the same lattice parameters as the 0.91Co/CeO<sub>2</sub> sample (Table 1), the intensity of the satellite peak was substantially lower. Hence, different oxide/hydroxide-like Co compounds, including those in Co–Ce–O solid solution, have been formed on the surface of the 0.91Co/CeO<sub>2</sub> sample. In particular, Co(OH)<sub>2</sub> in this case could result from hydration of highly dispersed species.

The Ni 2p<sub>3/2</sub> peak at 856.3 eV in the 2.7Ni/Al<sub>2</sub>O<sub>3</sub>-1200 sample (Fig. 4b) can be due to both NiAl<sub>2</sub>O<sub>4</sub> (BE ranging from 855.2 to 857.2 eV) and Ni(OH)<sub>2</sub> (855.6–856.6 eV),<sup>41–45</sup> the former being detected as well by XRD (Fig. 1, Table 1). NiO state, characterized by lower BE value (854.2 eV),<sup>45</sup> was detected in the 0.91Ni/CeO<sub>2</sub> sample together with Ni(OH)<sub>2</sub> (NiO:Ni(OH)<sub>2</sub> = 1:1) resulting in the widening of both the main Ni 2p peak and the energy shake-up satellite peak about 6 eV above the main one. As in the 0.91Co/CeO<sub>2</sub> sample, Ni(OH)<sub>2</sub> detection could indicate the presence of highly dispersed NiO species both in Al<sub>2</sub>O<sub>3</sub> and CeO<sub>2</sub>-based samples. In this case, their relative content in the samples is higher compared with the Co case.

While the BE value of the Fe 2p<sub>3/2</sub> spectra in the 0.86Fe/CeO<sub>2</sub> sample at 710.4 eV (Fig. 4c) indicates a preferential Fe<sup>3+</sup> state in the oxide, its high energy shift (BE = 711.8 eV) detected in both the 2.5Fe/Al<sub>2</sub>O<sub>3</sub>-1200 specimen and all Al<sub>2</sub>O<sub>3</sub>-1000, Al<sub>2</sub>O<sub>3</sub>-1200 and Al<sub>2</sub>O<sub>3</sub>-C supported samples can be related to formation of Fe<sup>3+</sup> oxyhydroxide.<sup>46</sup> In the 3.8Fe/Ce/Al<sub>2</sub>O<sub>3</sub> sample, both states of Fe<sup>3+</sup> have been detected also, but the fraction of Fe<sup>3+</sup> state in the oxide is somewhat higher than in Fe/Al<sub>2</sub>O<sub>3</sub>-based samples. Therefore, FeO<sub>x</sub> species anchor both to the Al<sub>2</sub>O<sub>3</sub> and CeO<sub>2</sub> surfaces.

In the Ce 3d spectra of the 3.8Fe/Ce/Al<sub>2</sub>O<sub>3</sub> sample, the normal complex form due to shake-down satellites from an O 1s to Ce 4f electron transfer observed for CeO<sub>2</sub> and 0.86Fe/CeO<sub>2</sub> was supplemented by the features marked as v' and u' due to anion defects and Ce<sup>3+</sup> (Fig. S2†).<sup>47</sup> This means that besides

smaller crystallized CeO<sub>2</sub> species, X-ray amorphous CeAlO<sub>3</sub> and probably isolated Ce<sup>3+</sup> species can reasonably form after CeO<sub>2</sub> precipitation onto high surface area alumina,<sup>48,49</sup> thus stabilizing alumina toward the formation of low surface area phases, as proposed in reference.<sup>27</sup>

Therefore, spinel-like surface structures including Al have been formed on the surface of the 2.7Co/Al<sub>2</sub>O<sub>3</sub>-1200 sample and probably their mixture with Ni(OH)<sub>2</sub> in the 2.7Ni/Al<sub>2</sub>O<sub>3</sub>-1200 sample. It is quite reasonable to suppose that above 700 °C, surface Fe oxyhydroxide formed after Fe supporting onto Al<sub>2</sub>O<sub>3</sub> and all Ni- and Co-containing hydroxylated species convert to corresponding oxides, and thus similar types of surface compounds participate in the reaction in both Al<sub>2</sub>O<sub>3</sub>-1200, CeO<sub>2</sub> and CeO<sub>2</sub>/Al<sub>2</sub>O<sub>3</sub> based samples.

Table 3 lists the data on the surface concentration of Me in the different Al<sub>2</sub>O<sub>3</sub>-1200 and CeO<sub>2</sub> based samples. Similar values were measured in the (2.5–2.7)Me/Al<sub>2</sub>O<sub>3</sub>-1200 and 0.91Co(0.86Fe)/CeO<sub>2</sub> samples with the same as related per surface unit ( $6.7 \times 10^{19}$  at m<sup>-2</sup>) content of Me therein that means similar MeO<sub>x</sub> (Co–Al–O) species dispersion ( $D_{Me}$ ) therein. Its relative value can be estimated as follows:  $D_{Me} = Me_s/C_{Me}$ , where  $Me_s$  is the surface atomic concentration of Me in the sample as measured by XPS (Table 3) [%] and  $C_{Me}$  is total content of Me in the samples [atoms/m<sup>2</sup>]. Noticeably higher content of Ni in the near surface layers of the CeO<sub>2</sub> based sample can be explained either by lower degree of Ni penetration into CeO<sub>2</sub>, resulting in the formation of Ni–Ce–O solid solutions (Table 2) or by higher dispersion of NiO<sub>x</sub> species, which agrees well with high content of hydroxylated species.

### 3.4. <sup>18</sup>O SSITKA

Fig. 5 shows the time dependencies of exchanged oxygen for different samples as related to unit of the surface ( $N_O$ ) calculated using the formulae

$$N_O = N_A \frac{2C_{O_2}U}{S_{BET}g} \int_0^t (\alpha_g^{input} - \alpha_g) dt$$

where  $\alpha_g^{input}$ —isotope fraction in the inlet mixture (0.95),  $C_{O_2}$  – O<sub>2</sub> concentration (mol mol<sup>-1</sup>),  $U$ —flow rate of the reaction mixture (mole/s), and  $N_A$ —Avogadro number. It is seen that for (2.5–2.7)Fe(Co)/Al<sub>2</sub>O<sub>3</sub>-1200 samples,  $N_O(t)$  dependencies (at higher rate of exchange on 2.5Fe/Al<sub>2</sub>O<sub>3</sub>-1200, as determined from the slope of  $N_O$  curves) reached the plateau after about 15 s after isotope admission corresponding to exchanged  $4.9 \times 10^{20}$  and  $3.2 \times 10^{20}$  O atoms per g for 2.5Fe/Al<sub>2</sub>O<sub>3</sub>-1200 and 2.7Co/Al<sub>2</sub>O<sub>3</sub>-1200 samples, respectively. Taking account of the quantity of supported Me ( $2.7 \times 10^{20}$  atoms per g), one can suppose that within the accuracy of measurement, solely the oxygen of Fe<sub>2</sub>O<sub>3</sub> and Co oxidic compounds (Co<sub>3</sub>O<sub>4</sub> + Co<sub>3-x</sub>Al<sub>x</sub>O<sub>4</sub>) participated in the exchange. The integral quantity of exchanged oxygen in the 2.5Fe/Al<sub>2</sub>O<sub>3</sub>-C sample ( $7.9 \times 10^{20}$  atoms per g) substantially exceeds that in supported Fe oxide. Provided substantially more dispersed FeO<sub>x</sub> species have been formed in this sample compared with those in



**Table 3** Physicochemical properties of different Me/Al<sub>2</sub>O<sub>3</sub>, Me/CeO<sub>2</sub> and 3.8Fe/Ce/Al<sub>2</sub>O<sub>3</sub> samples

Sample	S <sub>BET</sub> , m <sup>2</sup> g <sup>-1</sup>	Me <sub>s</sub> , at% (by XPS)	Fe <sub>exp</sub> , rel. units	D <sub>Me</sub> , rel. units
CeO <sub>2</sub> based				
0.86Fe/CeO <sub>2</sub>	1.3	1.0	1.3	1.5
0.91Co/CeO <sub>2</sub>	1.3	1.2	—	1.8
0.91Ni/CeO <sub>2</sub>	1.3	2.0	—	2.7
2.5Fe/CeO <sub>2</sub>	1.3	1.5	2.1	0.72
Al <sub>2</sub> O <sub>3</sub> -1200 and Al <sub>2</sub> O <sub>3</sub> -1000 based				
2.5Fe/Al <sub>2</sub> O <sub>3</sub> -1200	4	1.1	4.4	1.6
2.7Co/Al <sub>2</sub> O <sub>3</sub> -1200	4	1.0	—	1.5
2.7Ni/Al <sub>2</sub> O <sub>3</sub> -1200	4	1.4	—	2.1
0.86Fe/Al <sub>2</sub> O <sub>3</sub> -1200	4	1.1	4.4	4.8
2.5Fe/Al <sub>2</sub> O <sub>3</sub> -1000	7	1.4	9.8	3.7
Al <sub>2</sub> O <sub>3</sub> -C based				
2.5Fe/Al <sub>2</sub> O <sub>3</sub> -C	61	0.46	28.1	10.5
6.6Fe/Al <sub>2</sub> O <sub>3</sub> -C	46	1.3	59.8	8.5
13.2Fe/Al <sub>2</sub> O <sub>3</sub> -C	33	2.2	72.6	5.1
19.8Fe/Al <sub>2</sub> O <sub>3</sub> -C	22	1.6	35.2	1.7
CeO <sub>2</sub> /Al <sub>2</sub> O <sub>3</sub> based				
3.8Fe/CeO <sub>2</sub> /Al <sub>2</sub> O <sub>3</sub>	50	1.3	65.0	16.0

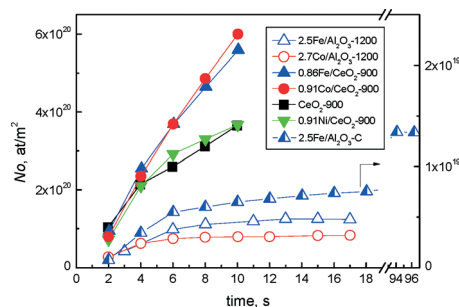
2.5Fe/Al<sub>2</sub>O<sub>3</sub>-1200 one (Table 3), it is more probably support oxygen that can transfer to O<sub>2</sub> molecule through developed Fe-alumina interface.

Substantially more profound and faster oxygen exchange took place on CeO<sub>2</sub> based samples, obviously involving the bulk of the support starting from the very low time after <sup>18</sup>O<sub>2</sub> admission. The rate of exchange changed in the following order: 0.91Co/CeO<sub>2</sub> ≥ 0.86Fe/CeO<sub>2</sub> > 0.91Ni/CeO<sub>2</sub> ≈ CeO<sub>2</sub> and correlated with values of the red shift of the CeO<sub>2</sub> band gap energy (*E<sub>g</sub>*) in turn depending on the content of Me–Ce mixed solution in the sample characterized by increased degree of disorder. Therefore, oxygen transfer from fluorite lattice to the surface by extended vacancies arising after insertion of Me<sup>n+</sup> ions into the fluorite lattice can be responsible for enforced rate of isotope exchange on Me/CeO<sub>2</sub> (Me = Co, Fe) samples compared with pure CeO<sub>2</sub>.

### 3.5. Catalytic activity

#### 3.5.1. N<sub>2</sub>O decomposition

*Effect of the support nature.* Among Al<sub>2</sub>O<sub>3</sub>-1200-based samples with similar surface concentration as supported Me

**Fig. 5** Time dependence of the quantity of exchanged oxygen (*N<sub>O</sub>*) in <sup>18</sup>O SSITKA experiments for different Me/Al<sub>2</sub>O<sub>3</sub> and Me/CeO<sub>2</sub> samples.

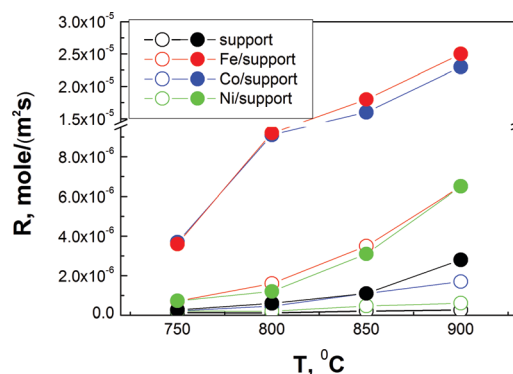
( $6.7 \times 10^{19}$  at m<sup>-2</sup>), catalytic activity in N<sub>2</sub>O decomposition at *T* = 750–900 °C can be ordered as follows: 2.5Fe/Al<sub>2</sub>O<sub>3</sub>-1200 > 2.7Co/Al<sub>2</sub>O<sub>3</sub>-1200 > 2.7Ni/Al<sub>2</sub>O<sub>3</sub>-1200 > Al<sub>2</sub>O<sub>3</sub>-1200 (Fig. 6). The (0.86–0.91)Me/CeO<sub>2</sub> samples with quite close, both calculated ( $6.7 \times 10^{19}$  at m<sup>-2</sup>) and real (Table 3), surface concentration of Me as in (2.5–2.7)Me/Al<sub>2</sub>O<sub>3</sub>-1200 samples revealed substantially higher intrinsic activity. In the case of Co and Ni containing samples such increase of the activity could be partly related to the formation of principally different state of active component (oxides/hydroxides in CeO<sub>2</sub> instead of corresponding Co(Ni)–Al–O spinels located on the surface of Al<sub>2</sub>O<sub>3</sub>). Nevertheless, a similar effect observed for Fe based samples characterized by similar type of active species on both supports obviously points to the importance of increased oxygen mobility of CeO<sub>2</sub>, which in turn was substantially more active than Al<sub>2</sub>O<sub>3</sub>. The general scheme of N<sub>2</sub>O decomposition obeys the *Langmuir–Hinshehwood mechanism*:



where S is surface active site, N<sub>2</sub>O-S is adsorbed or chemisorbed N<sub>2</sub>O, and O-S is adsorbed or chemisorbed O, the rate of O<sub>2</sub> desorption by step 3) in the case of (0.86–0.91) Me/CeO<sub>2</sub> samples increases due to alternative fast supply of oxygen to reduced site S from the subsurface layers (O<sub>ss</sub>) of CeO<sub>2</sub> characterized by increased bulk oxygen mobility through Me–CeO<sub>2</sub> interface containing many oxygen vacancies to obtain additional O-S site:



A similar scheme considering two alternative pathways of regeneration of active sites was also proposed for Cu/CeO<sub>2</sub> samples tested in substantially lower temperature range

**Fig. 6** Temperature dependence of the activity of different (2.5–2.7) Me/Al<sub>2</sub>O<sub>3</sub>-1200 (open symbols) and (0.86–0.91) Me/CeO<sub>2</sub> (solid symbols) samples (Me = Co, Fe, Ni) in the reaction of N<sub>2</sub>O decomposition.



(between 300 and 550 °C) and included recombination step (if two oxidized copper sites are close enough to each other) and the step of  $\text{Cu}^{2+}$ -O-species reduction by  $\text{Ce}^{3+}$ .<sup>50</sup>

**Effect of Fe content and  $\text{FeO}_x$  dispersion.** With variation of Fe content in  $\text{Al}_2\text{O}_3$ -1200-based samples from 0.89 to 6.6 wt% (Fe was chosen as the most active among Me) we observed the inverse “activity (as related both to sample surface unit and to one Fe atom) – Fe content” dependence (Fig. 7A). The same  $\text{Fe}_s$  values for 0.86Fe/ $\text{Al}_2\text{O}_3$ -1200 and 2.5Fe/ $\text{Al}_2\text{O}_3$ -1200 samples (Table 3) indicate decrease of  $\text{FeO}_x$  species dispersion ( $D_{\text{Fe}}$ , Table 3) at higher Fe content. Finally, similar rates of  $\text{N}_2\text{O}$  decomposition were measured for bulk  $\text{Fe}_2\text{O}_3$  and all Fe/ $\text{Al}_2\text{O}_3$ -1200 samples (Fig. S3†), although in the former case the  $\text{Fe}_s$  value should be obviously higher. Therefore, activity of surface Fe sites decreases substantially with enlargement of  $\text{FeO}_x$  species.

With variation of Fe content in  $\text{CeO}_2$ -based samples from 0.5 to 2.5 wt% (i.e. at similar interval of supported Fe to that in the case of  $\text{Al}_2\text{O}_3$ -1200-based samples as related per surface unit and thus similar dispersion of  $\text{FeO}_x$  species) their higher activity due to increased mobility of oxygen is more prominent at lower quantity of supported Fe. However, activity drop was substantially more prominent, although even higher  $\text{Fe}_s$  values were measured for the 2.5Fe/ $\text{CeO}_2$  sample than for the 0.86Fe/ $\text{CeO}_2$  one (Table 3). Supposing the rate of oxygen transfer from the bulk to active sites should depend on the length of  $\text{MeO}_x$ - $\text{CeO}_2$  interface, its decrease at enlargement of  $\text{FeO}_x$  species (Table 3), revealed as start of oxygen exchange at higher temperature (Fig. S4†) should make an additional negative contribution to the activity.

**Effect of the support surface area.** In accordance with observed effect of  $\text{FeO}_x$  dispersion on activity, use of the support characterized by higher specific surface area allows obtaining more dispersed  $\text{FeO}_x$  species at substantially higher total Fe content (Table 3). This opens up additional possibilities for increase of conversion as measured at the same sample loading. Indeed, at a similar quantity of supported Fe,  $\text{N}_2\text{O}$  conversion increased with  $S_{\text{BET}}$  value of  $\text{Al}_2\text{O}_3$  (Fig. 7B).

Unfortunately, for Fe/ $\text{Al}_2\text{O}_3$ -C samples we failed to perform catalytic tests at reasonably low conversion values for correct

calculation of the reaction rate values. This fact and substantial negative effect of the quantity of supported Fe on  $S_{\text{BET}}$  value (Tables 2 and 3) complicated analysis of parameters determining the activity. To overcome this problem, we calculated the concentration of exposable  $\text{FeO}_x$  species ( $\text{Fe}_{\text{exp}}$ ) per weight unit by the following formula:  $\text{Fe}_{\text{exp}} = \text{Fe}_s \cdot S_{\text{BET}}$ , where  $\text{Fe}_s$  is the surface concentration of Fe as measured by XPS (Table 3), and compared conversion values were measured for the same catalyst loading as dependent on both Fe content in the sample and  $\text{Fe}_{\text{exp}}$ . It turned out that  $\text{N}_2\text{O}$  conversion decreased with increase of Fe content from 2.5% to 19.8% (Fig. 7B) or  $\text{FeO}_x$  dispersion drop (Table 3), but this order cardinally differed from that for  $\text{Fe}_{\text{exp}}$  ( $13.2\text{Fe}/\text{Al}_2\text{O}_3\text{-C} > 6.6\text{Fe}/\text{Al}_2\text{O}_3\text{-C} > 19.8\text{Fe}/\text{Al}_2\text{O}_3\text{-C} > 2.5\text{Fe}/\text{Al}_2\text{O}_3\text{-C}$ ). Therefore, similar to Fe/ $\text{Al}_2\text{O}_3$ -1200 samples, it is the size effect of  $\text{FeO}_x$  species that seems to be the dominant factor determining descending character of “conversion-Fe content” dependence. Similar reverse dependence was already observed earlier for lower (500–650 °C) temperatures.<sup>51</sup> Taking account of SSITKA data obtained for 2.5Fe/ $\text{Al}_2\text{O}_3$ -1200 and 2.5Fe/ $\text{Al}_2\text{O}_3$ -C samples, higher activity of smaller  $\text{FeO}_x$  species can be due to growing ability of oxygen supply to reduced active sites S from the alumina regions adjacent to developed  $\text{MeO}_x$ -alumina interface (step 4). Oxygen (3 vol%) and  $\text{H}_2\text{O}$  (3 vol%) addition into the reaction mixture, in accordance with considered abovementioned scheme of the mechanism, decreased the observed  $\text{N}_2\text{O}$  conversion, but did not change the order of activity (Fig. S5†).

**Effect of  $\text{CeO}_2$  dispersion.** Using the effect of high oxygen mobility of  $\text{CeO}_2$  for the increase of the efficiency of  $\text{N}_2\text{O}$  decomposition (Fig. 7B) is restricted by its low surface area under the reaction conditions.<sup>3,20</sup> Therefore, in addition to traditionally used increase of concentration of active sites by supporting more active component, we tried to disperse  $\text{CeO}_2$  by supporting onto high surface area  $\text{Al}_2\text{O}_3$ . Only Fe oxide was used in this case to avoid formation of low active Ni (Co)-Al spinels. The 3.8Fe/Ce/ $\text{Al}_2\text{O}_3$  and 9.9Fe/Ce/ $\text{Al}_2\text{O}_3$  samples revealed that the highest  $\text{N}_2\text{O}$  conversion (Fig. 7B) was due to the part of  $\text{FeO}_x$  that was anchored to the surface of higher dispersed ceria particles (Table 1, Fig. 4c). At the same time, the size effect, at least for the sample 3.8Fe/Ce/ $\text{Al}_2\text{O}_3$ , cannot be completely excluded (compare  $D_{\text{Fe}}$  values in the Table 3 for the samples 3.8Fe/Ce/ $\text{Al}_2\text{O}_3$  and 6.6Fe/ $\text{Al}_2\text{O}_3$ -C with similar  $S_{\text{BET}}$ ).

### 3.5.2. $\text{NH}_3$ oxidation

**Effect of the support nature.** Among (2.5–2.7) Me/ $\text{Al}_2\text{O}_3$ -1200 samples, the 2.5Fe/ $\text{Al}_2\text{O}_3$ -1200 one was the most active (Fig. 8A) and characterized by the highest selectivity to  $\text{NO} + \text{NO}_2$  (86–88%). As a result, the orders for the activity and the efficiency of  $\text{NO}_x$  formation evaluated as  $\text{NO}_x \text{ yield} = \text{Conversion} \times \text{NO}_x \text{ selectivity}$  were similar to that for the activity of  $\text{N}_2\text{O}$  decomposition:  $2.5\text{Fe}/\text{Al}_2\text{O}_3\text{-1200} \gg 2.7\text{Co}/\text{Al}_2\text{O}_3\text{-1200} > 2.7\text{Ni}/\text{Al}_2\text{O}_3\text{-1200} > \text{Al}_2\text{O}_3\text{-1200}$ . In addition, the  $\text{N}_2\text{O}$  yield value calculated in a similar manner as for  $\text{NO}_x \text{ yield}$  on the 2.5Fe/ $\text{Al}_2\text{O}_3$ -1200 sample in this temperature interval was lower than 2%, which is comparable to that for

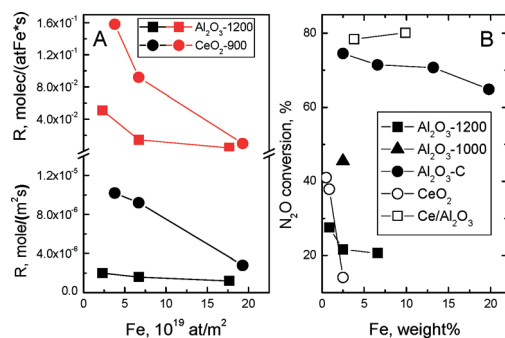


Fig. 7 Reaction rate (A) and  $\text{N}_2\text{O}$  conversion as measured at the same sample loading and flow rate (B) at 800 °C depending on Fe content in  $\text{Al}_2\text{O}_3$ -1200,  $\text{Al}_2\text{O}_3$ -1000,  $\text{Al}_2\text{O}_3$ -C,  $\text{CeO}_2$  and Ce/ $\text{Al}_2\text{O}_3$  based samples.



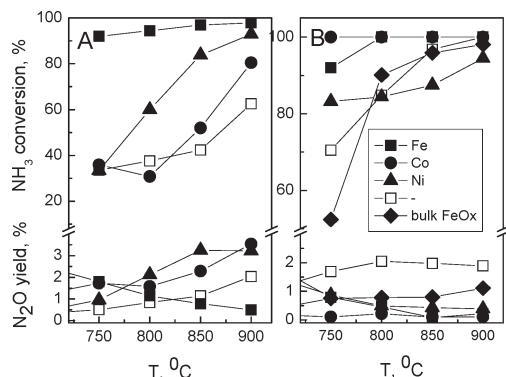


Fig. 8 Temperature dependence of  $\text{NH}_3$  conversion and  $\text{N}_2\text{O}$  yield for (2.5–2.7)  $\text{Me}/\text{Al}_2\text{O}_3$ -1200 (A) and (0.86–0.91)  $\text{Me}/\text{CeO}_2$ -900 (B) samples. Catalyst loading 0.015 g.

$\text{Pt-Rh}$  gauzes,<sup>1</sup> while continuous increase of  $\text{N}_2\text{O}$  yield with temperature was noted for all other samples. At lower  $\text{O}_2$  concentration in the inlet mixture (2.5%), the yield of  $\text{NO}_x$  decreased to 77–78%, mainly because of lower selectivity. For Co- and Ni-based samples and for pure  $\text{Al}_2\text{O}_3$ -1200, negative changes of conversion and  $\text{NO}_x$  selectivity were substantially more prominent.

We failed to calculate the rate of ammonia oxidation in all temperature intervals due to non-differential reactor operating conditions. Hence, to compare intrinsic activity of samples characterized by different  $S_{\text{BET}}$  values, we tested catalytic properties of (0.86–0.91)  $\text{Me}/\text{CeO}_2$  samples at catalyst loading of 0.043 g corresponding to the same surface area as for  $\text{Al}_2\text{O}_3$ -1200-based samples. In these conditions, at 750 °C, complete  $\text{NH}_3$  conversion was measured on all (0.86–0.91)  $\text{Me}/\text{CeO}_2$  samples, and 96% for  $\text{CeO}_2$  that is obviously due to capability of  $\text{CeO}_2$  itself to donate lattice oxygen for ammonia oxidation.<sup>16</sup> Even at the same catalyst loading as for  $\text{Al}_2\text{O}_3$ -1200-based samples (0.015 g), *i.e.* at about a 3 times lower number of Me sites therein (Table 3), higher values of  $\text{NH}_3$  conversion were observed for corresponding  $\text{CeO}_2$  based samples (Fig. 8B). This increase, at least in the case of Fe-based samples, is exclusively due to the ability of the support to donate oxygen to  $\text{FeO}_x$ , since substantially lower conversion values were measured on  $\text{CeO}_2$  and bulk  $\text{FeO}_x$  characterized by similar  $S_{\text{BET}}$  values.  $\text{N}_2\text{O}$  yield values were reasonably lower than on corresponding  $\text{Al}_2\text{O}_3$ -1200-based samples. In addition, at 800 °C, the order of  $\text{NH}_3$  conversion and  $\text{NO}_x$  yield (not shown for brevity),  $0.91\text{Co}/\text{CeO}_2 \geq 0.86\text{Fe}/\text{CeO}_2 > 0.91\text{Ni}/\text{CeO}_2 \approx \text{CeO}_2$ , was exactly the same as for the efficiency towards oxygen exchange therein (Fig. 4).

Strong decrease of both  $\text{NH}_3$  oxidation<sup>52</sup> and  $\text{N}_2\text{O}$  decomposition<sup>32</sup> over Co oxide at high temperatures was shown to be due to  $\text{Co}_3\text{O}_4$  reduction to  $\text{CoO}$ . We did not observe such deactivation of the 0.91 $\text{Co}/\text{CeO}_2$  sample with temperature both at  $\text{N}_2\text{O}$  decomposition (Fig. 6), as in  $\text{Co}_3\text{O}_4$ - $\text{CeO}_2$  mixed oxides with low Co content,<sup>11</sup> and at ammonia oxidation (Fig. S7B†), although  $\text{Co}_3\text{O}_4$  reduction under TPD conditions was observed (Fig. S6†). It obviously can be explained by higher resistance of the Co–Ce interface towards reduction due to

some oxygen supply from  $\text{CeO}_2$  by reaction (4). Nevertheless, at lower temperature, the 0.91 $\text{Co}/\text{CeO}_2$  sample with Co state closer to  $\text{Co}_3\text{O}_4$  was already substantially more active than 0.87 $\text{Fe}/\text{CeO}_2$  both in  $\text{N}_2\text{O}$  decomposition (Fig. S7A†) and  $\text{NH}_3$  oxidation (Fig. S7B†).

**Effect of Fe content and  $\text{FeO}_x$  dispersion.** Decreasing dependence of  $\text{NH}_3$  conversion *vs.* Fe content in  $\text{Al}_2\text{O}_3$ -1200 and  $\text{CeO}_2$ -based samples (0.015 g sample loading for all these experiments) was observed (Fig. 9), similarly to the reaction of  $\text{N}_2\text{O}$  decomposition, and thus can be related to size effect. Moreover, for the  $\text{Fe}/\text{CeO}_2$  case, it was more prominent due to attenuation of oxygen transfer processes through the Fe– $\text{CeO}_x$  interface (Fig. S4†). Nevertheless, unlike the reaction of  $\text{N}_2\text{O}$  decomposition,  $\text{FeO}_x$  dispersion is not a predominant factor for  $\text{NH}_3$  conversion any more. Therefore, at Fe content lower than  $3 \times 10^{19}$  atoms per  $\text{m}^2$  (the case with  $\text{Fe}/\text{Al}_2\text{O}_3$ -C and  $\text{Fe}/\text{Ce}/\text{Al}_2\text{O}_3$  samples), the  $\text{NH}_3$  conversion value depended mainly on the quantity of exposable Fe ( $\text{Fe}_{\text{exp}}$ ).

At the same time, these were larger  $\text{FeO}_x$  species that converted  $\text{NH}_3$  to  $\text{NO}_x$  more selectively in all  $\text{Al}_2\text{O}_3$ -based samples (Fig. S8†), finally resulting in quite similar (77–81%, in the case of  $\text{Fe}/\text{Al}_2\text{O}_3$ -1200 samples) or growing with Fe content (up to 79% for  $\text{Fe}/\text{Al}_2\text{O}_3$ -C)  $\text{NO}_x$  yield values (Fig. 9). In accordance with findings of Pérez-Ramírez and Kondratenko<sup>16</sup> on bulk  $\text{Fe}_2\text{O}_3$ , the desired reaction follows a Mars–van Krevelen-type scheme involving the participation of lattice oxygen in the  $\text{NH}_3$  conversion to  $\text{NO}$ . The degree of reduction of the oxide surface was shown to determine the product distribution. One can reasonably suppose that for small species, the  $\text{FeO}_x$  surface should be in a more reduced state because of a smaller rate of dissociative activation of  $\text{O}_2$  molecules on the Fe–Al interface. In addition, a growing contribution from low selective  $\text{NH}_3$  oxidation on  $\text{Al}_2\text{O}_3$  should be accounted as well.

We also believe that the more oxidized state of  $\text{FeO}_x$  anchored to  $\text{CeO}_2$ , resulting from more efficient O transfer through the Fe–Ce interface, causes higher selectivity to  $\text{NO}_x$  in the 3.8 $\text{Fe}/\text{Ce}/\text{Al}_2\text{O}_3$  and 9.9 $\text{Fe}/\text{Ce}/\text{Al}_2\text{O}_3$  samples compared to the  $\text{Fe}/\text{Al}_2\text{O}_3$ -C ones with similar dispersion. In addition, substantially smaller values of  $\text{N}_2\text{O}$  yield were measured on

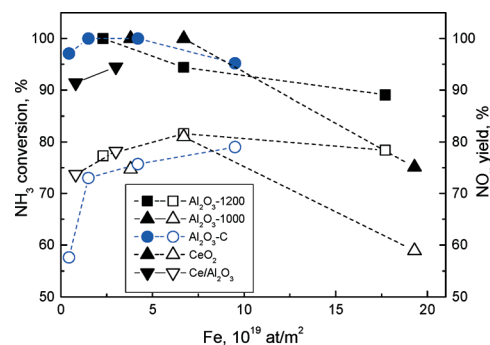


Fig. 9 Dependence of  $\text{NH}_3$  conversion (solid symbols) and  $\text{NO}_x$  yield (open symbols) on Fe content in different  $\text{Fe}/(\text{Al}_2\text{O}_3, \text{CeO}_2)$  samples. Catalyst loading 0.015 g.



Fe/Ce/Al<sub>2</sub>O<sub>3</sub> samples, which agree with their higher activity towards N<sub>2</sub>O decomposition.

## Conclusions

We have shown that replacement of Al<sub>2</sub>O<sub>3</sub> by CeO<sub>2</sub> as the support for MeO<sub>x</sub> (Me = Fe, Co, Ni) characterized by increased lattice oxygen mobility resulted in substantial increase of the rates of <sup>16</sup>O/<sup>18</sup>O exchange at 800 °C, N<sub>2</sub>O decomposition and NH<sub>3</sub> oxidation on corresponding samples. Oxygen transfer from the fluorite lattice to the surface by extended oxygen vacancies arose after insertion of Me<sup>n+</sup> ions into the fluorite lattice was shown to be responsible for the enforced rate of isotope exchange.

Formation of low active spinel-like Me–Al–O structures restricted the application of Co and Ni oxides in any Al<sub>2</sub>O<sub>3</sub> containing catalysts. For CeO<sub>2</sub>- and Al<sub>2</sub>O<sub>3</sub>-based samples with supported FeO<sub>x</sub>, an obvious size effect was observed in both reactions. Therefore, highly dispersed FeO<sub>x</sub> was substantially more active due to change of contribution of oxygen supply from the support (both ceria and, probably, alumina) to reduced surface sites through Fe–CeO<sub>x</sub> interface thus increasing the rate of O<sub>2</sub> desorption. However, smaller species oxidized NH<sub>3</sub> to NO<sub>x</sub> less selectively.

Using high surface area Al<sub>2</sub>O<sub>3</sub>-C, the samples with high content of dispersed FeO<sub>x</sub> in the weight unit were synthesized to increase observable N<sub>2</sub>O conversion. To increase the surface area of CeO<sub>2</sub> and thus efficiently use the promoting effect of oxygen mobility, CeO<sub>2</sub> was dispersed onto alumina by precipitation. Fe/Ce/Al<sub>2</sub>O<sub>3</sub> samples with optimal content of Fe revealed superior activity in N<sub>2</sub>O decomposition and NH<sub>3</sub> oxidation to NO<sub>x</sub> compared with Fe/Al<sub>2</sub>O<sub>3</sub> with similar *S*<sub>BET</sub> and dispersion of FeO<sub>x</sub> species values.

## Acknowledgements

The authors thank Mrs. I. Kharina for preparation of the Al<sub>2</sub>O<sub>3</sub>-C sample.

## Notes and references

- 1 J. Pérez-Ramírez, F. Kapteijn, K. Schöffel and J. A. Moulijn, *Appl. Catal., B*, 2003, **44**, 117.
- 2 P. Granger, P. Esteves, S. Kieger, L. Navascues and G. Leclercq, *Appl. Catal., B*, 2006, **62**, 236.
- 3 P. Esteves, Y. Wu, C. Dujardin, M. K. Dongare and P. Granger, *Catal. Today*, 2011, **176**, 453.
- 4 D. V. Ivanov, E. M. Sadovskaya, L. G. Pinaeva and L. A. Isupova, *J. Catal.*, 2009, **267**, 5.
- 5 Y. Wu, X. Ni, A. Beaurain, C. Dujardin and P. Granger, *Appl. Catal., B*, 2012, **125**, 149.
- 6 D. V. Ivanov, L. G. Pinaeva, L. A. Isupova, E. M. Sadovskaya, I. P. Prosvirin, E. Yu Gerasimov and I. S. Yakovleva, *Appl. Catal., A*, 2013, **457**, 42.
- 7 J. Pérez-Ramírez and M. Santiago, *Chem. Commun.*, 2007, 619.
- 8 G. Giecko, T. Borowiecki, W. Gac and J. Kruk, *Catal. Today*, 2008, **137**, 403.
- 9 J. Kruk, K. Stolecki, K. Michalska, M. Konkol and P. Kowalik, *Catal. Today*, 2012, **191**, 125.
- 10 E. Wilczkowska, K. Krawczyk, J. Petryk, J. W. Sobczak and Z. Kaszukur, *Appl. Catal., A*, 2010, **389**, 165.
- 11 E. Iwanek, K. Krawczyk, J. Petryk, J. W. Sobczak and Z. Kaszukur, *Appl. Catal., B*, 2011, **106**, 416.
- 12 M. Konsolakis, *ACS Catal.*, 2015, **5**, 6397.
- 13 V. A. Sadykov, L. A. Isupova, I. A. Zolotarskii, L. N. Bobrova, A. S. Noskov, V. N. Parmon, E. A. Brushtein, T. V. Telyatnikova, V. I. Chernyshev and V. V. Lunin, *Appl. Catal., A*, 2000, **204**, 59.
- 14 L. Pinaeva, E. Sutormina, L. Isupova, N. Kulikovskaya and A. Marchuk, *RU Pat.*, 2 430 782 C1, 2010.
- 15 L. Pinaeva, L. Isupova, I. Prosvirin, E. Sadovskaya, I. Danilova, D. Ivanov and E. Gerasimov, *Catal. Lett.*, 2013, **143**, 1294.
- 16 J. Pérez-Ramírez and E. Kondratenko, *J. Catal.*, 2007, **250**, 240.
- 17 M. Zabitskiy, B. Eravec, P. Djinić and A. Pintar, *Chem. Eng. J.*, 2014, **254**, 153.
- 18 M. Konsolakis, S. A. C. Carabineiro, E. Papista, G. E. Marnellos, P. B. Tavares, J. Agostinho Moreira, Y. Romaguera-Barcelay and J. L. Figueiredo, *Catal. Sci. Technol.*, 2015, **5**, 3714.
- 19 L. Isupova, Yu. Tanashev, I. Kharina, E. Moroz, G. Litvak, N. Boldyreva, E. Paukshtis, E. Burgina, A. Budneva, A. Shmakov, N. Rudina, V. Kruglyakov and V. Parmon, *Chem. Eng. J.*, 2005, **107**, 163.
- 20 I. Danilova, E. Slavinskaya, V. Zaikovskii, A. Ivanova, A. Boronin, R. Gulyaev and Yu. Amosov, *Kinet. Catal.*, 2010, **51**, 143.
- 21 J. Tauc, R. Grigorovici and A. Vancu, *Phys. Status Solidi B*, 1966, **15**, 627.
- 22 V. Malakhov, N. Boldyreva, A. Vlasov and L. Dovlitova, *J. Anal. Chem.*, 2011, **66**, 458.
- 23 L. G. Pinaeva, E. M. Sadovskaya, A. P. Suknev, V. B. Goncharov and B. S. Bal'zhinimaev, in *Mass Spectrometry Handbook*, ed. M. S. Lee, Wiley, Hoboken, 2012, pp. 1229–1256.
- 24 S. Kurajica, J. Popović, E. Tkalčec, B. Gržeta and V. Mandić, *Mater. Chem. Phys.*, 2012, **135**, 587.
- 25 O. Kirichenko, V. Ushakov, E. Moroz and M. Vorob'eva, *Kinet. Catal.*, 1993, **34**, 739.
- 26 Z. Zhang, D. Han, S. Wei and Y. Zhang, *J. Catal.*, 2010, **276**, 16.
- 27 A. Gupta, A. Kumar, U. V. Waghmare and M. S. Hegde, *Chem. Mater.*, 2009, **21**, 4880.
- 28 A. Piras, S. Colussi, A. Trovarelli, V. Sergo, J. Llorca, R. Psaro and L. Sordelli, *J. Phys. Chem. B*, 2005, **109**, 11110.
- 29 A. Bensalem, J. C. Muller and F. Bozon-Verduraz, *J. Chem. Soc., Faraday Trans.*, 1992, **88**, 153.
- 30 R. Zhang, J. T. Miller and C. D. Baertsch, *J. Catal.*, 2012, **294**, 69.
- 31 R. C. Olegário, E. C. F. Souza, J. F. M. Borges, J. B. M. Cunha, A. V. C. Andrade, S. R. M. Antunes and A. C. Antunes, *Dyes Pigm.*, 2013, **97**, 113.



- 32 C. He, M. Paulus, W. Chu, J. Find, J. A. Nickl and K. Kohler, *Catal. Today*, 2008, **131**, 305.
- 33 I. G. Casella and M. R. Guascito, *J. Electroanal. Chem.*, 1999, **476**, 54.
- 34 H. Xiong, Y. Zhang, K. Liew and J. Li, *J. Mol. Catal. A: Chem.*, 2005, **231**, 145.
- 35 M. H. Kim and K.-H. Choo, *Catal. Commun.*, 2007, **8**, 462.
- 36 J. Yang, H. Liu, W. N. Martens and R. L. Frost, *J. Phys. Chem.*, 2010, **C114**, 111.
- 37 X. Duan, M. Pan, F. Yu and D. Yuan, *J. Alloys Compd.*, 2011, **509**, 1079.
- 38 N. Srisawad, W. Chaitree, O. Mekasuwandumrong, P. Praserttham and J. Panpranot, *J. Nanomater.*, 2012, **2012**, 1.
- 39 D. Barreca and C. Massignam, *Chem. Mater.*, 2001, **13**, 588.
- 40 S. C. Petitto, E. M. Marsh, G. A. Carson and M. A. Langell, *J. Mol. Catal. A: Chem.*, 2008, **281**, 49.
- 41 D. Nikolova, R. Edreva-Kardjieva, G. Gouliev, T. Grozeva and P. Tzvetkov, *Appl. Catal., A*, 2006, **297**, 135.
- 42 P. Dufresne, E. Grimblot and J. P. Bonnelle, *J. Phys. Chem.*, 1981, **85**, 2344.
- 43 E. Laurent and B. Delmon, *J. Catal.*, 1994, **146**, 281.
- 44 C. Jiménez-González, Z. Boukha, B. de Rivas, J. J. Delgado, M. A. Cauqui, J. R. González-Velasco, J. I. Gutiérrez-Ortiz and R. López-Fonseca, *Appl. Catal., A*, 2013, **466**, 9.
- 45 P. Prieto, V. Nistor, K. Nouneh, M. Oyama, M. Abd-Leftil and R. Diaz, *Appl. Surf. Sci.*, 2012, **258**, 8807.
- 46 S. Suzuki, K. Yanagihara and K. Hirokawa, *Surf. Interface Anal.*, 2000, **30**, 372.
- 47 L. Chen, P. Fleming, V. Morris, J. D. Holmes and M. A. Morris, *J. Phys. Chem. C*, 2010, **114**, 12909.
- 48 J. Z. Shyu, W. H. Weber and H. S. Gandhi, *J. Phys. Chem.*, 1988, **92**, 4964.
- 49 C. Ge, L. Liu, Z. Liu, X. Yao, Y. Cao, C. Tang, F. Gao and L. Dong, *Catal. Commun.*, 2014, **51**, 95.
- 50 M. Zabilskiy, P. Djinoić, E. Tchernychova, O. Tkachenko, L. Kustov and A. Pintar, *ACS Catal.*, 2015, **5**, 5357.
- 51 P. Pomonis, D. Vattis, A. Lycourghiotis and C. Kordulis, *J. Chem. Soc., Faraday Trans. 1*, 1985, **81**, 2043.
- 52 M. C. Goromonzi, S. K. Raman, B. D. Padalia, A. Manohar and P. N. Koul, *React. Kinet. Catal. Lett.*, 1980, **15**, 131.

